Nanoscale Res Lett (2007) 2:417–429
DOI 10.1007/s11671-007-9078-0

NANO REVIEW

Submonolayer Quantum Dots for High Speed Surface Emitting Lasers

N. N. Ledentsov · D. Bimberg · F. Hopfer · A. Mutig · V. A. Shchukin · A. V. Savel'ev · G. Fiol · E. Stock · H. Eisele · M. Dähne · D. Gerthsen · U. Fischer · D. Litvinov · A. Rosenauer · S. S. Mikhrin · A. R. Kovsh · N. D. Zakharov · P. Werner

Received: 10 May 2007 / Accepted: 18 July 2007 / Published online: 10 August 2007
© to the authors 2007

Abstract We report on progress in growth and applications of submonolayer (SML) quantum dots (QDs) in high-speed vertical-cavity surface-emitting lasers (VCSELs). SML deposition enables controlled formation of high density QD arrays with good size and shape uniformity. Further increase in excitonic absorption and gain is possible with vertical stacking of SML QDs using ultrathin spacer layers. Vertically correlated, tilted or anticorrelated arrangements of the SML islands are realized and allow QD strain and wavefunction engineering. Respectively, both TE and TM polarizations of the luminescence can be achieved in the edge-emission using the same constituting materials. SML QDs provide ultrahigh modal gain, reduced temperature depletion and gain saturation effects when used in active media in laser diodes. Temperature robustness up to 100 °C for 0.98 μm range vertical-cavity surface-emitting lasers (VCSELs) is realized in the continuous wave regime. An open eye 20 Gb/s operation with bit error rates better than 10^{-12} has been achieved in a temperature range 25–85 °C *without current adjustment*. Relaxation oscillations up to $\sim$30 GHz have been realized indicating feasibility of 40 Gb/s signal transmission.

Keywords Quantum dots · Nanophotonics · Semiconductor lasers · Surface-emitting lasers · Self-organized growth

A. V. Savel'ev—on leave from the Abraham Ioffe Physical Technical Institute, Politekhnicheskaya 26, 194021, St. Petersburg, Russia.

N. N. Ledentsov (✉)
VI System GmbH, Berlin, Germany
e-mail: leden@sol.physik.tu-berlin.de

N. N. Ledentsov · D. Bimberg · F. Hopfer · A. Mutig · V. A. Shchukin · A. V. Savel'ev · G. Fiol · E. Stock · H. Eisele · M. Dähne
The Institut für Festkörperphysik, Technische Universität Berlin, Hardenbergstr. 36, 10623 Berlin, Germany

D. Gerthsen · U. Fischer · D. Litvinov · A. Rosenauer
Universität Karlsruhe, 76128 Karlsruhe, Germany

S. S. Mikhrin · A. R. Kovsh
NL-Nanosemiconductor (Innolume) GmbH, Konrad-Adenauer-Allee 11, 44263 Dortmund, Germany

N. D. Zakharov · P. Werner
Max-Planck-Institut für Mikrostrukturphysik, Weinberg 2, 06120 Halle, Germany

Introduction

Presently, data traffic crossing optical fiber networks increases three orders of magnitude per decade [1]. To cope with this increase, there exists a growing demand in adding more channels per a single link, increasing the bit rate per link and installing new links. The maximum commercial single-channel data transmission rate is increasing 4-fold each 5 years. In telecom-range systems it entered 40 Gb/s transmission range with 100 Gb/s to come in the nearest future. External intensity modulation is used in telecom transmitters to match both speed and spectral and beam quality requirements. In datacom, however, where the bit rate has already entered the 10 Gb/s range, directly modulated devices are used due to cost requirements. Further significant increase in the bit rate in this approach is becoming more and more demanding, because of the extreme power densities in the cavity needed to match the requested time response.

Furthermore, high differential capacitance under forward bias, bit error rate (BER) requirements requesting a proportional power increase with the speed increase and the related high power consumption are limiting factors for the performance and competitiveness. At the same time the bit rate increase is also characteristic for copper electrical interconnects, where the market approached ~US$40B in 2006 with an annual growth rate of ~16%. As the attenuation of signal at 10 Gb/s makes cost-effective transmission through copper prohibitively expensive and complex at distances ~3–10 m, this segment is to be covered by optical interconnects at speeds higher 10 Gb/s. Fiber optic links based on vertical-cavity surface-emitting lasers (VCSELs) are broadly believed to be the best candidates [2–4] for these applications in the foreseeable future, however, the device performance must match the performance demand and respond the above listed challenges.

Moreover, lack of components, operating in a robust way even at 20 Gb/s in the requested temperature and BER ranges, raises questions concerning the further perspectives of the VCSEL technology. To respond the demands, directly modulated devices need to overcome the following challenges:

- a 4-fold increase in the modulation speed requires a 16-fold increase in the current density, assuming the similar device geometry (the relaxation oscillation frequency, characterizing the time-response of the active medium, scales with the square root of the power density in the laser cavity);
- a 4-fold increase in the modulation speed requests a proportional increase in the output power to provide the same power per pulse to keep the same BER. This translates to ~3 mW of "in-fiber" power for 40 Gb/s VCSELs;
- with transmission speed increase and the related ultrahigh power densities, the wavelength chirp, dynamic beam degradation, and spatial hole-burning are becoming pronounced, deteriorating the optical transmission, even in case where single mode devices are used;
- increased current density results in a significant overheating and accelerated degradation rate, even when all the other parameters of the device are met.

A significant increase of the modulation speed of VCSELs combined with the demands for power, degradation robustness and speed of next generation ultrahigh speed systems require new material and device concepts.

This paper addresses VCSEL prospects in parts of using of novel types of submonolayer quantum dot (SML QD) active media [5], [6] capable to ultrahigh modal gain, keeping all the other key QD advantages in place, such as excitonic gain mechanism, suppressed carrier diffusion and low degradation rate. We underline also the role of the novel VCSEL design, which avoids dangerous parasitic cavity modes causing gain depletion, self-pulsation and radiative leakage.

We believe that further VCSEL development, being based on nanophotonic approaches, will ensure the necessary pace of the device performance to cope with the tasks of the decades to come.

Stranski-Krastanow Quantum Dot Gain Media

Lasing in self-organized Stranski-Krastanow QDs (SK-QDs) at room and low temperatures was reported in 1993 applying edge-emitting geometry and photopumped excitation [7]. Soon after (1994) current injection lasing in QDs [8] up to 300 K was reported. In 1995 injection lasing in QDs at 80 K with the threshold current density of 815 A/cm^2 [9–11] was observed. SK-QDs have been also used in the active region of VCSELs [12]. In 1996 high-performance VCSELs based on vertically coupled QDs have been realized [13] by MBE and, later, MOCVD [14]. Later, however, the main interest has shifted towards long-wavelength 1.3 μm devices. Indeed, the first-ever GaAs-based VCSEL emitting beyond 1.3 μm was realized using SK InAs QDs [15]. There has been a lot of activities to improve the device. However, in spite of the fact that the basic performance at room temperature in the CW mode was significantly improved [16], high-temperature operation and high-speed modulation remained a big issue, opposite to 1300 nm-range edge-emitters based on the same epitaxial QD material [16], [17]. Low modulation bandwidth [16], [18] and insufficient temperature robustness [18] appeared to be a problem for 1.3 μm GaAs SK-QD VCSELs. More recently, a new explosion of interest, also for 850–1,100 nm spectral range occurred, being sparked by the need to extend dramatically the speed of directly modulated devices for optical interconnects, but avoid the risk of device degradation. The extreme robustness of edge-emitting QD lasers to degradation [19], [20] and the temperature stability of their characteristics [21], [22] motivated the research.

Growth of QDs Using Submonolayer Deposition

Submonolayer (SML) deposition of lattice mismatched material results in dense arrays of nanoscale two-dimensional islands [23]. Submonolayer deposition on vicinal surfaces was applied to form tilted superlattices [24] or single-sheet QD structures 25]. Later, formation of arrays of anisotropic InAs islands ordered in size and shape has been reported on terraces of misoriented GaAs surfaces

26]. A remarkable feature of SML islands is their weak carrier localization energy, which makes device applications at room temperature demanding. However, for II–VI materials with large electron and hole effective masses and, also, significant Coulomb interaction energy further enhanced by carrier localization, a lot of interesting options arises [27, 28]. After overgrowth with the matrix material, the deposition of the next SML insertion is controlled by the non-uniform lateral strain distribution caused by the underlying strained islands and different types of correlated structures can be formed [29].

The spontaneous formation of ordered arrays of islands has been studied theoretically and experimentally for a long time (see, e. g., a review in [30]). The formation of ordered ("parquet") structures on crystal surfaces has been shown to occur if two phases with different values of intrinsic surface stress (τ_{ij}) coexist on the surface [23]. The surface of the crystal is intrinsically stressed due to the necessity to follow the lattice parameter of the bulk where the atom arrangement is different. If the values of this surface stress are different for the two phases co-existing on the crystal surface (heteroepitaxial deposits, domains of surface reconstruction, adsorbate phases, etc.), formation of boundaries will always result in some elastic energy relaxation (Fig 1) of the more stressed phase along the boundaries between the domains, making ripening of the domains energetically unfavorable. For strained 2D islands there always exists a total energy minimum for a particular island size [23, 30].

At finite temperature the island size distribution somewhat broadens [31], and another peak in the island size distribution appears near the zero island size, corresponding to the finite concentration of free adatoms and their associates on the surface. The mean size and density of the equilibrium islands decrease with increasing substrate temperature [31]. At very high temperatures only the peak in the size distribution curve at zero island size survives and the island size dispersion becomes very pronounced.

In Fig. 2 equilibrium distribution of the number of atoms in 2D islands as a function of substrate temperature is shown [31]. The optimum island at $T = 0$ consists of $N_0 = 625$ atoms, and the surface coverage is 0.1. With temperature increase, more atoms are transferred to a phase of mobile adatoms existing on the surface. The equilibrium island size decreases and the island density decreases as well.

In Fig. 3 we show processed cross-section high-resolution transmission electron microscopy (HRTEM) images of InAs submonolayer insertions in a GaAs matrux. The lateral size of the InAs-rich domains formed at 480 °C is

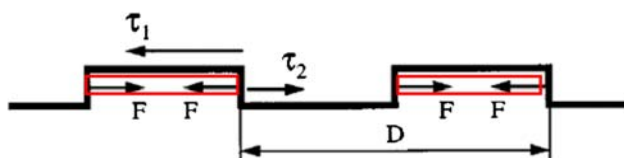

Fig. 1 Two phases with different values of intrinsic surface stress (τ_{ij}) coexist on the surface. If the values τ_{ij} are different, there exists a resulting elastic relaxation force F, which causes the lattice displacement to reduce the energy of the system. Thus, formation of boundaries becomes energetically favorable unless short-range potential due to dangling bonds at the edges starts to play a role. Thus, an optimal size of the island exists

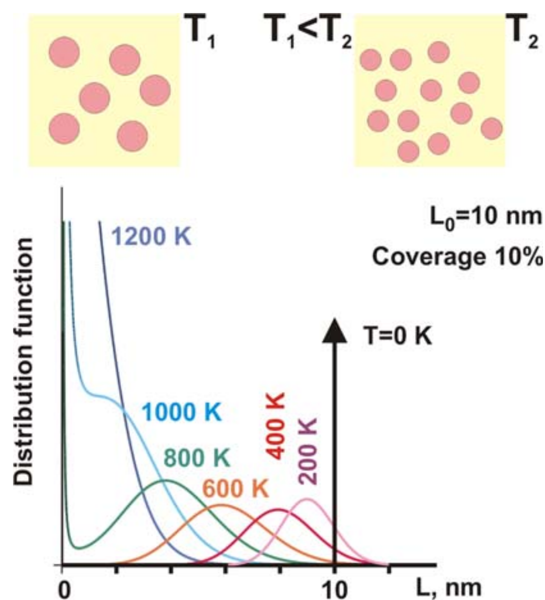

Fig. 2 Equilibrium distribution of the number of atoms 2D islands. The optimum island at $T = 0$ consists of $N_0 = 625$ atoms, and the surface coverage is 0.1

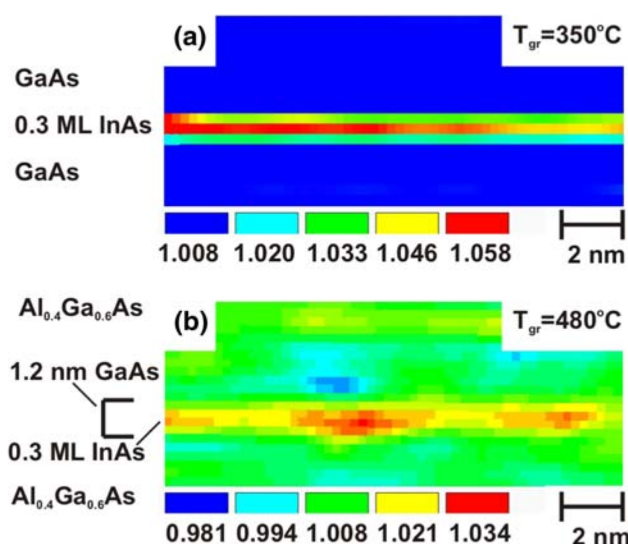

Fig. 3 Processsed HRTEM image of 0.3 ML InAs deposit in a GaAs matrix at 350 °C (**a**) and 480 °C (**b**)

close to 2–3 nm being in general agreement with the data reported [26] for InAs submonolayer deposits on GaAs. Deposition at lower temperature results in lateral sizes of 6–8 nm in a general agreement with theory.

As the localization energy of SML QDs is relatively small, their stacking appears to be particularly important.

In Fig. 4 we show results of theoretic modeling of the preferable arrangement of 2D-shaped islands in an elastically anisotropic media. A phase diagram of a double sheet array of flat islands (right, Fig. 4) is shown. *P* is the ratio of the force applied to buried islands in different directions, z_0 is the separation between the surface and the sheet of buried islands, and *D* is the in-plane period. One can see that for thinner spacers the growth occurs in predominantly vertically correlated way, or in tilted arrangement. However, already at periods close to one half of the lateral period, a transition to anticorrelated growth occurs [6, 30]. At larger spacer layer thicknesses, the correlated growth is to dominate again, but at thicker spacers both the degree of vertical alignment and the strength of electronic coupling are dramatically reduced. Thus, vertically correlated growth can be realized for SML QDs only at extremely thin spacer layers.

In Fig. 5 we show HRTEM (a) and processed HRTEM (b) images of stacked InAs 0.5 ML islands inserted into a 1.2 nm GaAs layer in an $Al_{0.4}Ga_{0.6}As$ matrix at 490 °C. One can see from the image that the islands can be observed only after image-processing, which reveals the local lattice parameter in the vertical direction. One can see that the islands do not form clearly vertically correlated arrangement in the range of the spacer thicknesses chosen.

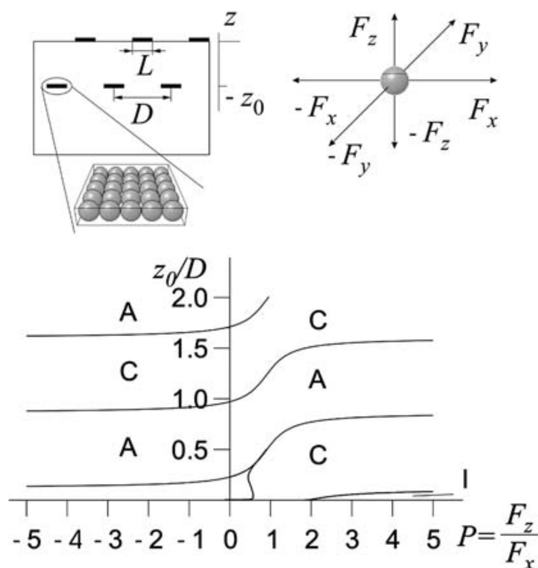

Fig. 4 Modeling of the preferable arrangement of 2D-shaped islands in an elastically-anisotropic media. A phase diagram of a double sheet array of flat islands (left) is shown. *P* is the ratio of the force applied to buried islands in different directions, z_0 is the separation between the surface and the sheet of buried islands, and D is the in-plane period. C- denotes correlated arrangement, A-anticorrelated and I-intermediate (tilted) arrangement

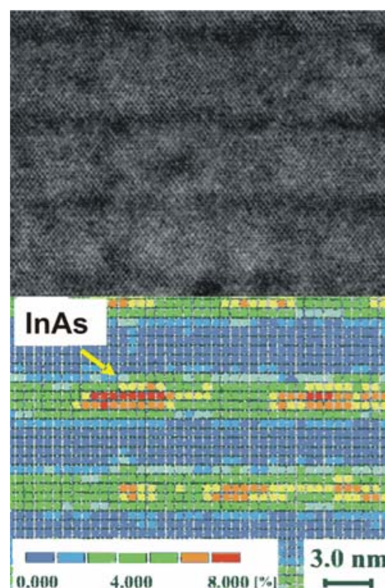

Fig. 5 HRTEM (**a**) and processed HRTEM (**b**) images of stacked InAs 0.5 ML islands inserted into a 1.2 nm GaAs layer in an $Al_{0.4}Ga_{0.6}As$ matrix. (b) shows a color-coded map of the local increase of the lattice parameter in the vertical direction. Substrate temperature is 490 °C

In spite of the fact that the lateral dimensions of SML QDs are small and the related strain fields are weak, these QDs can be revealed in plan-view TEM images, giving a possibility to judge on their lateral density and relative lateral sizes, revealed by the associated strain fields. Plan-view TEM images of InAs 0.5 ML islands inserted into a 1.2 nm GaAs layer clad into an $Al_xGa_{1-x}As$ matrix and stacked with a 5 nm periodicity are shown in Fig. 6 for (a) $Al_{0.4}Ga_{0.6}As$ matrix and (b) $Al_{0.6}Ga_{0.4}As$ matrix. The lateral density of SML QDs (~ 1–2×10^{11} cm^{-2}) is much higher as compared to conventional Stranski-Krastanow QDs deposited in similar conditions. The lateral sizes (overestimated by strain fields) are significantly lower (<10 nm), respectively.

Anticorrelated arrangement of SML QDs was first clearly revealed for CdSe QDs in a ZnSe matrix, as it is shown in Fig. 7. Significant extension of the strain fields of SML islands can be seen in Fig. 7b in the total lattice displacement map, which evidences the 2D-like shifted flat pedestal regions on top of the islands. Thus, the strain gradient regions are mostly concentrated at the edges of these pedestals, making the anti-correlated or tilted growth arrangement favorable.

The actual distribution of the material in SML islands is different from the nominal one due to the finite adatom concentration on the surface and diffusion- and

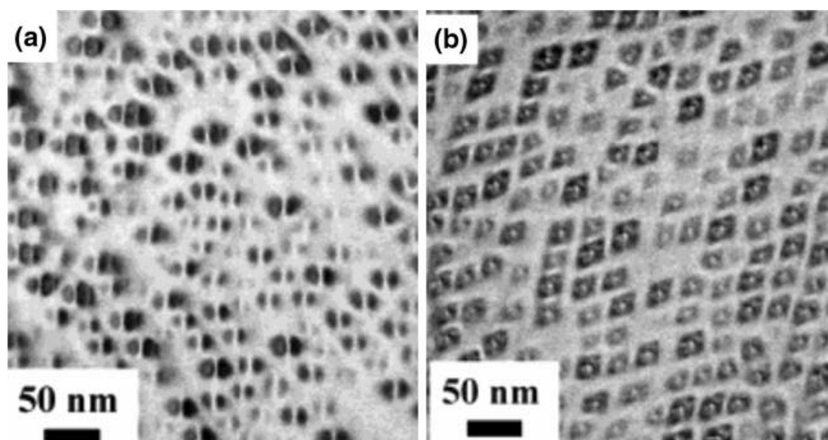

Fig. 6 InAs 0.5 ML islands inserted into a 1.2 nm GaAs layer clad into an $Al_xGa_{1-x}As$ matrix and stacked with a 5 nm period. (**a**) $Al_{0.4}Ga_{0.6}As$ matrix (**b**) $Al_{0.6}Ga_{0.4}As$ matrix

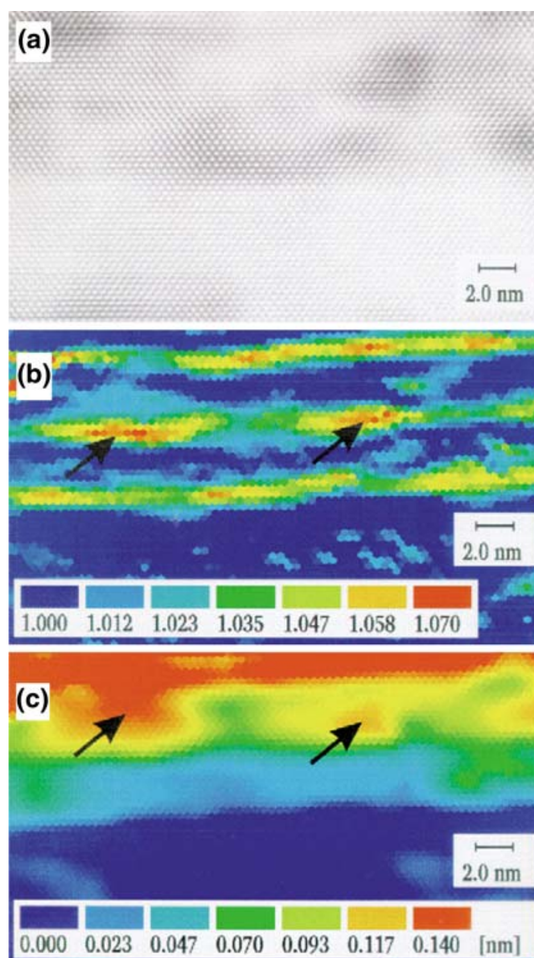

Fig. 7 (**a**) <110> projection HRTEM image of a CdSe/ZnSe submonolayer (SML) superlattice structure. (**b**) Color-coded maps of the local lattice parameter in the vertical <001> direction and (**c**) the total atom displacements with respect to the underlying ZnSe layer plane for the same area

segregation-induced intermixing. In HRTEM experiments, averaging effects along the HRTEM foil used in measurements is taking place. Thus, careful comparison of modeled and experimental results is needed to judge on real material distribution. In Fig. 8 color-coded local lattice parameter (a,c) and total lattice displacement maps modeled for anticorrelated arrangement of 2D islands are shown. By comparison of the experimental image in Fig. 7 with the modeling data in Fig. 8 and assuming significant averaging due to the small lateral island size as compared to the HRTEM foil ($\sim$15 nm), one may conclude that the actual CdSe composition of SML islands is at or higher than 40% and the adatom-induced "wetting layer" composition is 15–20% or lower.

Electronic Properties of Submonolayer QDs

Small lateral size of the islands formed by ultrathin insertions raises a question on the applicability of QD model to explain the properties of SML insertions. A clear signature of QD states is observation of discrete luminescence lines due to single QDs [28], which survive up to high temperatures.

In Fig. 9 we show cathodoluminescence spectra of CdSe QDs obtained using an approach of ultrasmall openings in metal masks. This technique had been used to resolve single QD emission lines up to high observation temperatures and to calculate the density of the QDs. A series of temperature dependent spectra of a single QD is displayed in Fig. 9a. Increasing the temperature enhances the probability of phonon-related dephasing processes, causing Lorentzian broadening of the lines above 50 K. For temperatures above 110 K the lines are still clearly resolved in the spectra while their wavelength overlap becomes more pronounced. The peak energy of single lines and of their overlap at higher temperatures followed the CdSe band-gap dependence up to room temperature, evidencing the fact that no change in the recombination mechanism took place and the same QD radiative recombination mechanism dominate at 300 K. A lineshape analysis showed that the

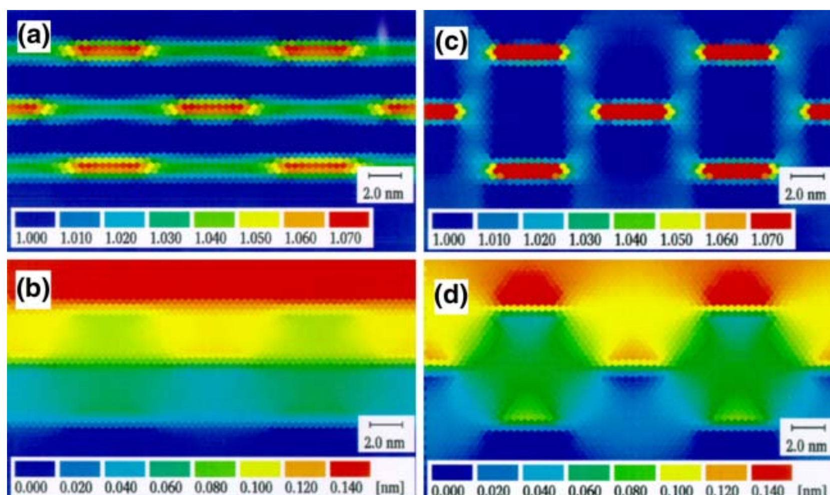

Fig. 8 Color-coded local lattice parameter (**a**, **c**) and total lattice displacement maps modeled for anticorrelated arrangement of 2D islands: 4 ML $Cd_XZn_{1-X}Se$ insertion (**a**, **b**) with $X_{island} = 0.4$, $X_{adatoms} = 0.2$; 3 ML $Cd_XZn_{1-X}Se$ (**c**, **d**) with $X_{island} = 1$, $X_{adatoms} = 0$

integrated intensity remained almost constant (see Fig. 9c) up to and above 100 K, while the amplitude decreased due to the dephasing-induced broadening. These observations suggest that thermal activation of QD excitons to continuum states is negligible even at temperatures above 100 K.

Another unique possibility, which was first discovered in SML QDs [29], and was later translated to SK QDs [32, 33] is a possibility to control polarization of the luminescence of QD structures in edge geometry. Indeed, vertically coupled growth results in strain and wavefunction modifications which favor unpolarized or even TM-polarized emission in edge geometry, opposite to the case of uncoupled QDs, always demonstrating TE-polarized emission, similar to the case of compressively strained or lattice-matched quantum wells.

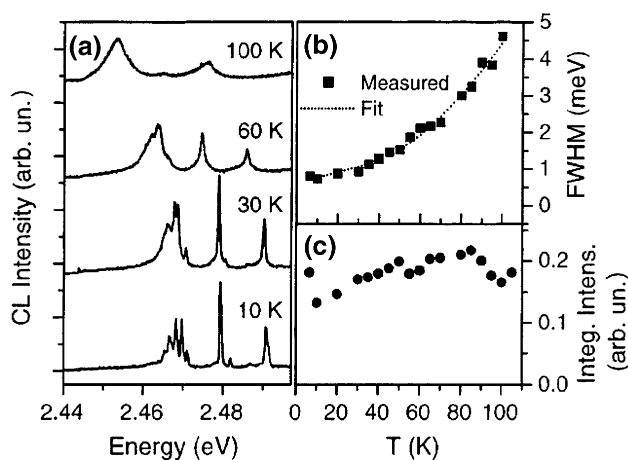

Fig. 9 (**a**) Emission spectra of an individual CdSe QD for different temperatures. (**b**) Temperature dependent linewidth of individual QD exciton lines. (**c**) Temperature dependent integrated intensities of individual QD exciton lines

In Fig. 10 we show color-coded maps of the local lattice parameter for SML QDs stacked with 3 nm (top) and 1.5 nm (bottom) spacer layers. One can see from Fig. 10 that transition to thinner spacers is accompanied by a remarkable change in the vertical correlation of the islands. Vertically aligned chains become clearly visible.

In Fig. 11 linearly polarized photoluminescence (PL) spectra of CdSe–ZnSe structures with 8, 3 and 1.5 nm ZnSe spacers measured in edge geometry are shown. The polarization changes from mostly TE for uncoupled islands (8 nm spacers) to mostly TM (accompanied by a red shift) for vertically coupled islands (1.5 nm spacers). The 3 nm spacer sample shows emission from both types of islands. Thus, formation of vertically correlated states is clearly confirmed in photoluminescence studies, on top of HRTEM results, evidencing the modification of the electronic spectrum of QDs.

It is also very important to note that the electron and hole confinement in vertically coupled QDs is significantly increased as compared to the wetting layer and matrix continuum, further improving temperature stability of the QD luminescence.

In the case of vertically correlated growth at very thin spacer layers, the surface morphology of the (In,Ga)As insertions becomes significantly affected, the dot size increases, and a periodic interface corrugation occurs.

The thickness and compositional modulation are revealed in this case in plan-view transmission electron microscopy (TEM) images (see Fig. 12a, c). In the case of anti-correlated or tilted arrangement of the islands, the interfaces remain planar, while the compositional modulation can be revealed in cross-section high-resolution transmission electron microscopy and in cross-section scanning tunneling microscopy (X-STM) [34]. In Fig. 13 we show a cross-section scanning tunneling microscopy image of SML QD insertions in chemically sensitive

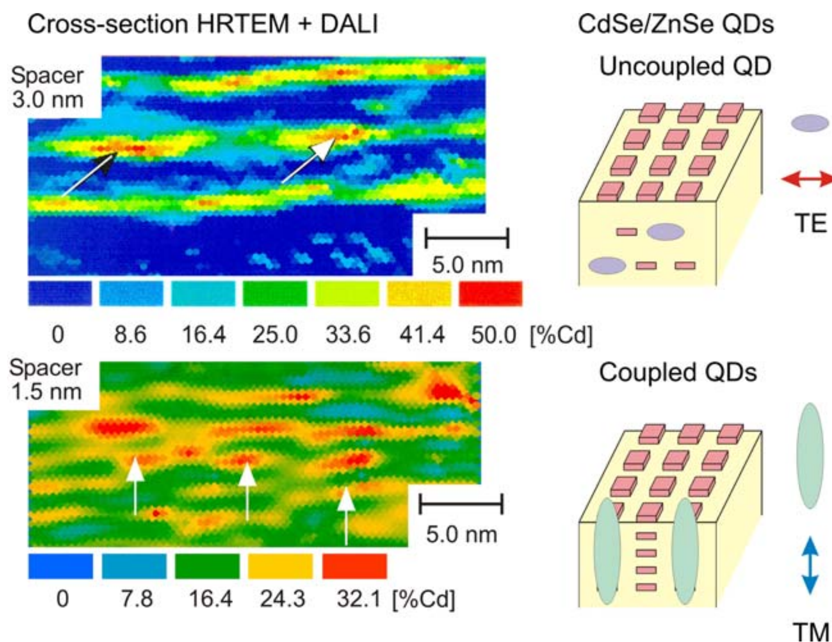

Fig. 10 Color-coded maps of the local lattice parameter for SML QDs stacked with 3 nm (top) and 1.5 nm(bottom) spacer layers. The relative arrangement of islands is shown schematically in the right figures in relation to edge luminescence polarization axes

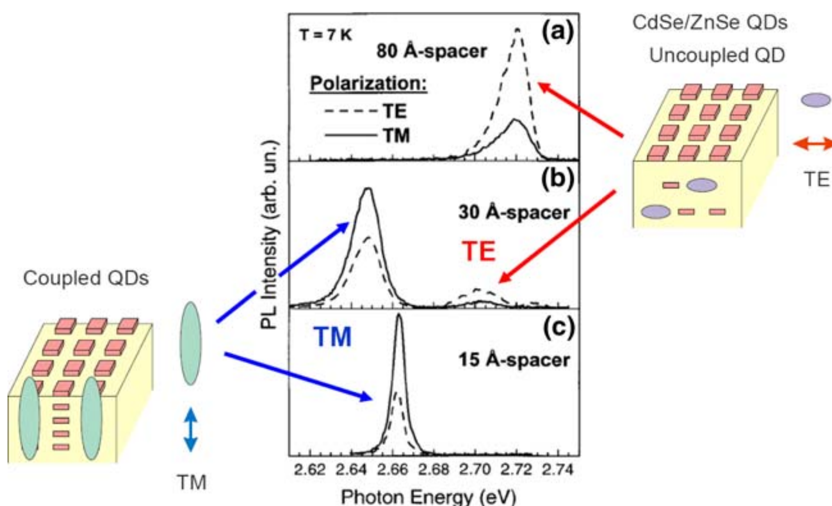

Fig. 11 Linearly polarized photoluminescence (PL) of structures with 8, 3 and 1.5 nm spacers measured in edge geometry. The polarization changes from mostly TE for uncoupled islands (8 nm spacers) to mostly TM (accompanied by a red shift) for vertically coupled islands (1.5 nm spacers). The 3 nm spacer sample shows emission from both types of islands. The relative arrangement of islands is shown schematically in the right figures in relation to edge luminescence polarization axes

conditions. Gray contrast corresponds to InAs SML regions, which are coupled into tilted chains. The tilted arrangement was theoretically predicted [35] and later observed for flat 2D-shaped QDs [36]. The horizontal lines correspond to single monolayer planes and the overall thickness of the insertion is ~7 nm. Thus, the SML deposition leads simultaneously to a significant lateral compositional modulation and high QD density [34], resulting in a high material and modal gain.

For ultrahigh-speed directly modulated VCSEL applications it is extremely important to create an active media, which is capable to ultrahigh modal gain at extremely high temperatures and current densities. The problem of conventional QW active media is the step-like density of states for intersuband transitions, which results in hole-burning effects at high current densities and gain depletion due to overheating. In spite of the fact that ultrahigh exciton oscillator strength can be realized in absorption spectra of QWs, the excitons do not play any positive role under the lasing conditions. At first, the excitons can be partially dissolved at room temperature. However, even in structures made of II–VI materials, where the exciton oscillator strength is high and the excitons dominate up to high excitation densities and observation temperatures, the predominant lasing mechanism is related to LO-phonon-assisted excitonic gain, which is relatively weak, as it comes from many-particle interactions (predominantly including an exciton and two LO-phonons). At high temperatures and excitation densities the excitons are heated and have a significant in-plane k-vector, making the

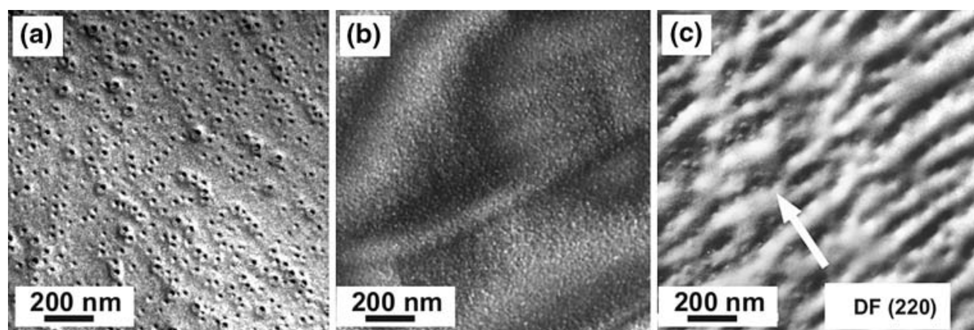

Fig. 12 Plan-view transmission electron microscopy (TEM) images of submonolayer QDs: Thicknesses of the insertions and the compostions are: (**a**) 5.4 nm, $In_{0.24}Al_{0.26}Ga_{0.48}As$; (**b**) 7.8 nm, $In_{0.19}Ga_{0.81}As$; (**c**) 5.4 nm $In_{0.24}Ga_{0.76}As$. Submonolayer deposition is performed in 0.8 ML InAs cycles (**a**, **c**), or in 0.5 ML (**b**) cycles. The characteristic feature size varies from 15–30 nm (**a**) to 5–15 nm (**b**) and 40–60 nm (**c**). Depending on the AlAs and InAs composition one can adjust the wavelength of SML QDs within 0.75–1.3 μm

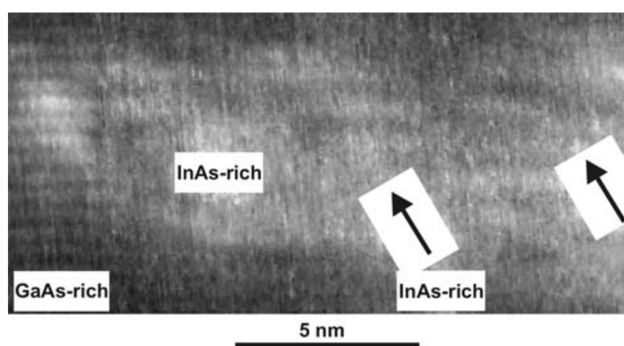

Fig. 13 Empty state cross-section scanning tunneling microscopy image of the SML QD insertion taken at low positive sample bias. Ten cycles of 0.5 ML InAs deposition cycles separated by 2.2 ML GaAs spacers at a substrate temperature of 490 °C has been deposited. 2–3 nm-wide In-rich columns tilted by $\sim 35^{o}$ with respect to [001] direction are observed

probability of their zero-phonon radiative annihilation negligibly low [5, 27, 28]. Already in narrow II–VI quantum wells, however, the interface roughness can make a zero-phonon scattering-assisted lasing mechanism dominant. A truly excitonic gain can be realized, however, only in QDs, where the excitons are fully confined. In practical QD structures, at least an order of magnitude higher material gain as compared to QWs at room temperature was manifested, even in case of significantly inhomogeneously broadened ensembles (>kT). The problem of using conventional S-K QDs in VCSELs originates, however, from the fact that the sheet density of QDs is relatively low $\sim 1\text{–}8 \times 10^{10}$ cm^{-2} and the carriers can escape from QDs at elevated temperatures populating the matrix and wetting layer states. Increasing the density of QDs by stacking is difficult due to the increased average strain in the structure and the related formation of misfit dislocations. As opposite, very small QDs formed by SML insertions can form efficient confinement centers of ultrahigh density, which can lift effectively the k-selection rule, but do not degrade the structural quality of the system. Pure exctionic lasing mechanism up to high temperatures and excitation densities can be realized on one side, while an ultrahigh density of QDs can be achieved on the other. Thus, gain coefficients comparable to the absorption coefficients in narrow QWs can be potentially, realized. To achieve this goal, however, one needs to keep the lateral size of the localizing insertions to be comparable or less than the effective exciton radius in the narrow QWs (about 5–8 nm). The confinement potential should be made as large as possible to provide the strongest confinement of the localized exciton with respect to the continuum states. The lateral separation between the localizing centers should be sufficient to prevent coupling of QD excitons to broad minizones staying above 3–5 nm, depending on the confinement potential (the size inhomogeneity may reduce the coupling even at very small average lateral separations). As a result of the above consideration, the material arrangement presented in Fig. 13 seems to be particularly interesting for applications in VCSELs.

Thus, in the case of the particular SML QDs used for the VCSEL structures processed and studied in this work, the SML growth proceeded in a mode with ten 0.5 ML InAs deposition cycles separated by 2.2 ML GaAs spacers at a substrate temperature of 490 °C. 10 s growth interruptions were introduced at the GaAs interfaces to ensure reproducible surface morphology for the InAs nucleation. Three sheets of stacked SML QD insertions separated by 13-nm-thick GaAs spacer layers were used as an active region [34].

In Fig. 14 we show photoluminescence (PL) and PL excitation (PLE) spectra of the SML QD structure, used in VCSELs, taken at 7 K. Two sharp peaks, separated by 12 meV with a full width at half maximum of $\sim$4–5 meV are observed in the PL spectra. The peak at lower energy dominates the spectra at low excitation densities (4 mW/cm^2), while the high-energy peak increases with higher

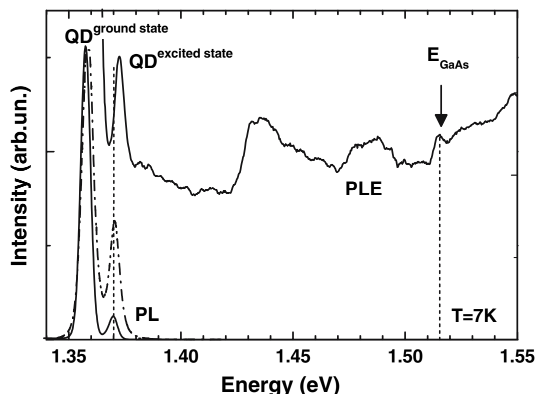

Fig. 14 Photoluminescence (PL) and PL excitation spectra of the SML QD structure. The PL spectra are taken at excitation densities of 4 mW/cm^2 (solid line) and $\sim$1 kW/cm^2 (dash-dotted line). The PLE spectrum is taken at 1.357 eV, which corresponds to the maximum of the PL intensity

excitation densities. PL excitation spectra evidence that both peaks originate from the same quantum object. The PLE spectra, detected at the lower energy peak reveals the higher energy peak, indicating that both states originate in the same quantum object. As the height of the SML insertion is only $\sim$7 nm, the double-peak feature can't be explained by the light-to-heavy hole exciton splitting due to the significant strain and quantum confinement-induced separation between the two valence band states [37]. The most natural assumption for the origin of the features is ground and excited heavy-hole QD exciton states, similar to the case of three-dimensional QDs [37].

Similarly, for the double-peak feature in the PLE spectra at 1.43 and 1.49 eV light-hole-like ground and excited exciton states might be responsible.

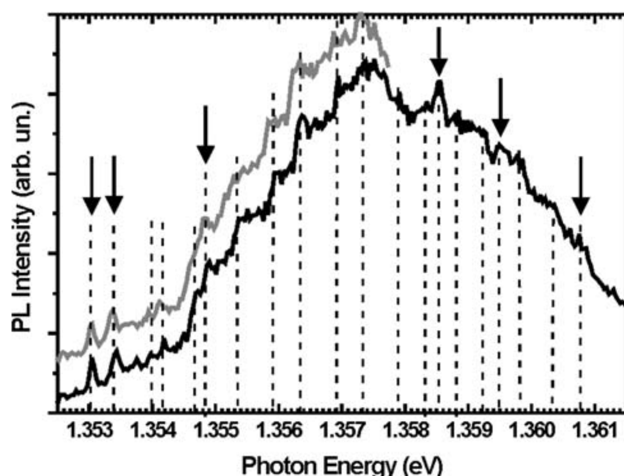

Fig. 15 Micro-PL spectra of the SML QD emission taken with an excitation spot of $\sim$1 μm^2 at T = 7 K. The gray line is the part of the PL spectrum repeated for the same excitation spot. The gray spectrum is shifted for clarity. One can see that all the main features in the spectra coincide

In Fig. 15 we show micro-PL spectra of the SML QDs taken with an excitation spot size of $\sim$1 μm^2. One can see that the PL spectrum is composed of multiple sharp lines originating from different SML QDs with narrow features resolved at both low and at high photon energy side of the spectrum [37]. The sharp emission lines are reproducible, once the micro-PL spectrum is repeated for the same spot (see gray line in Fig. 15). These sharp lines change, when the excitation spot on the sample is moved and can't be attributed to noise fluctuations. Similar features have been also revealed for the high-energy PL peak. Further studies are presently under way to achieve better understanding of the nature of the involved electronic states and optical properties of this type of SML QDs used in the VCSELs studied.

VCSEL Cavity Design

The radiative recombination probability of the dipole can be changed by changing the effective refractive index of the media to which the photon is emitted. Multilayer media open dramatic possibilities in redistribution of the oscillator strength, increase in the differential gain and suppression of the parasitic modes. The easiest approach to improve VCSEL device performance is to apply an antiwaveguiding design [38] with the cavity region having a smaller refractive index as compared to the average refractive index of the distributed Bragg reflectors (DBRs).

In conventional VCSELs, the cavity region is typically composed of the material having a higher refractive index. In this situation in-plane waveguide modes are possible. It is well known that VCSEL structures behave as low-threshold high-performance in-plane lasers, if processed in stripe-laser geometry. Assuming a standard high-speed oxide-confined VCSEL design with relatively small deep-etched VCSEL mesa, two types of *in-plane* confined modes, which do not penetrate into the DBRs, are possible. High quality factor (Q) modes are associated with the etched mesa, which is typically small enough to reduce the parasitic capacitance. Low-Q modes are associated with the oxide aperture [39]. As the VCSEL is operating under high current densities, the absorbing regions of the mesa, which are not electrically pumped by current injection become transparent by photoexitation due to in-plane spontaneous and stimulated emission.

These high Q modes behave as whispering gallery modes in microdisc structures, or, in some sense, similar to the modes existing in four-side facet-cleaved laser diodes. High power density accumulated in these modes can dramatically reduce the radiative lifetime and prevents low-threshold lasing for the VCSEL mode. Higher order high Q

whispering gallery modes penetrate deep into the VCSEL mesa up to the distance ~*R/n*, where *R* is the radius of the VCSEL mesa and *n* is the effective refractive index of the waveguide medium [39].

The whispering gallery modes associated with the oxide aperture is characterized by lower Q values due to the lower effective refractive index step in the outer region [39].

An approach to reduce such problems like radiative leakage, gain depletion, self-pulsation, or even parasitic in-plane lasing in VCSELs is the anti-waveguiding (AVCSEL) design, where no guided modes are possible for in-plane light propagation (see Fig. 16). The intensity of the guided mode is redistributed in this case towards tilted emission, which has low overlap with the active region and effectively leaks to the substrate. The AVCSEL concept is different to AlAs-rich half-wave cavity, previously used for creation of ultrahigh optical confinement oxide-confined VCSELs [40]. The AlAs-rich half-wave cavity designs may result in a low-loss in-plane mode with a significant overlap with the active layer. The mode is confined in the p-GaAs contact layer, which is sandwiched between the AlAs cavity on one side, and the dielectric Bragg reflector on the other. In the AVCSEL design such modes should be, preferably, avoided.

Further suppression of the parasitic tilted modes is possible in a multi-periodicity DBR VCSEL design, when the tilted modes can be suppressed by a second DBR periodicity.

Experimental Studies of 980 nm Sml QD Avcsels

Static Device Characteristics

The 980 nm VCSEL structures using InGaAs SML QDs, [34] were realized in an antiwaveguiding design [38, 39]

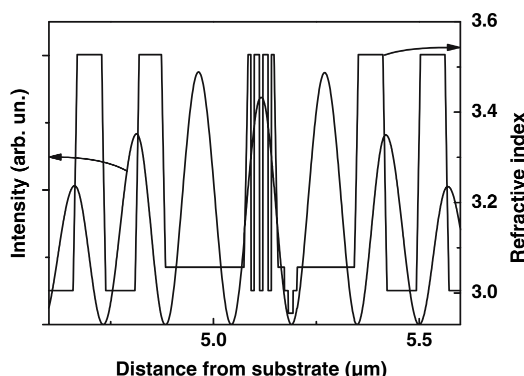

Fig. 16 Refractive index and superimposed intensity distribution for the central part of the SML QD-VCSEL

with a high Al-content cavity and doped bottom and top distributed Bragg reflectors with 32 and 19 pairs respectively (see Fig. 16). A single AlAs-rich aperture layer, being partially oxidized, was placed in a field intensity node on top of the $3\lambda/2$ cavity. High speed and high-efficiency devices with a co-planar layout were processed using standard lithographic, metal deposition and dry etching techniques. The selective oxidation procedure to create the oxide apertures was performed under carefully optimized conditions [34] to avoid formation of parasitic precipitates causing strain, degradation and increasing scattering loss in the devices.

Fig. 17 shows static continuous wave (cw) device characteristics for a 5 μm aperture multimode laser. The output power exceeds 10 mW at 20 °C; the differential efficiency and threshold current are hardly dependent on temperature over a very broad range.

Small Signal Modulation

For the small signal characterization the light was butt-coupled into a ~3 m 62.5 μm graded index multimode fiber, which was connected to a 25 GHz frequency calibrated multimode photoreceiver (Discovery Semiconductors DSC30 S). The small signal modulation as well as the recording of the frequency dependent transmission (S21) and reflection (S11) was done with a calibrated HP 8722 C 40 GHz network analyzer. Figure 18 shows small signal modulation parameters under continuous wave (cw) operation for a 6 μm SML QD-VCSEL at 25 and 85 °C, obtained from fitting the three-parameter transfer function with the unknown resonance frequency f_{res}, damping rate γ and parasitic cutoff frequency of the RC low-pass f_{par} to the S21 modulation response [41]. The maximum bandwidths (Fig. 10a) are 15 and 13 GHz, the modulation current efficiency factors are 4.6 and $5.6\,GHz/\sqrt{mA}$, respectively. Due to a smaller cavity-gain detuning at 85 °C for small currents, the modulation efficiency here is higher. The maximum thermally limited resonance frequency at 25 °C is close to $f_{res} = 10$ GHz, see Fig. 18b. The thermally limited modulation bandwidth would be ~15.5 GHz. Fig. 18c shows the damping rate vs. square of the resonance frequency. The K-factor is identical for both temperatures up to medium resonance frequencies and currents. Its value predicts an intrinsic bandwidth of $f_{damp} = 21$ GHz. From the different kink-points of the slope of the damping rate at both temperatures the influence of the temperature dependent differential gain on the damping rate can be inferred. The electrical RC-limited bandwidth is $f_{par} = 12$ GHz, obtained from equivalent circuit fitting to the measured S11-parameters. With negligible damping and no thermal

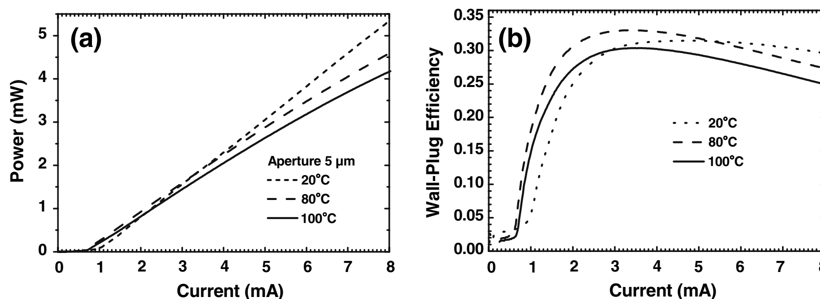

Fig. 17 Characteristics of a multimode SML-QD-AVCSEL: (**a**) *L-U-I* and (**b**) wall-plug efficiency and threshold current vs. temperature

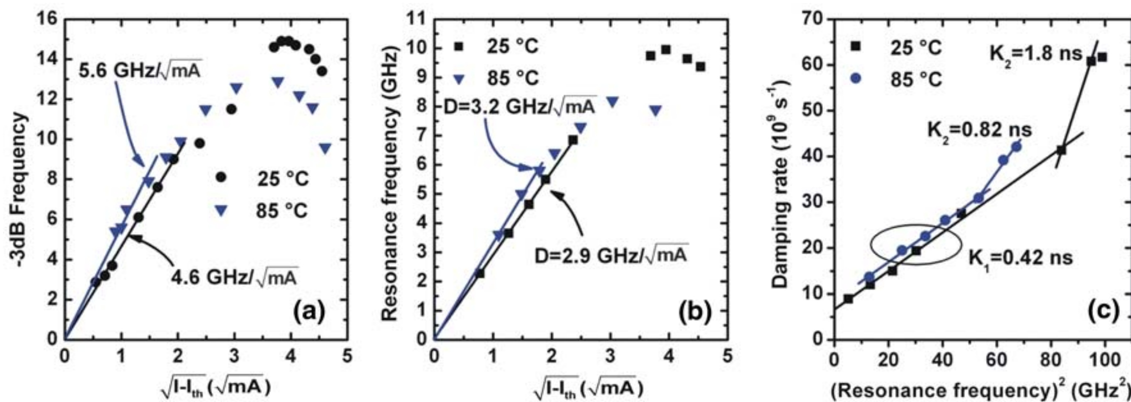

Fig. 18 Small signal modulation parameters for a 6 µm SML QD-VCSEL at 25 and 85 °C, obtained from fitting the modulation response to the three-parameter transfer function: (**a**)—3 dB bandwidth and (**b**) resonance frequency as a function of the square root of the current above threshold, (**c**) damping rate vs. squared resonance frequency. The maximum -3 dB bandwidth is 15 and 13 GHz, respectively

effects, this would result in a parasitic limited modulation bandwidth of $(2 + \sqrt{3}) \times f_{par}$ [42]. Damping is always present and the maximum parasitic limit is only reached for very high resonance frequencies of $f_r = \sqrt{(5 + 3\sqrt{3})} \times f_{par}$. One can conclude, that the resonance frequency and thus thermal effects dominate. Simulations of the transfer function with different values for f_{res}, γ and f_{par} also confirmed this condition. A small signal modulation bandwidth of 12 GHz has been reported in [43] for edge emitting QD lasers.

Large Signal Modulation

The same fibers and detector as for the small signal modulation experiments were used. Fig. 19a shows optical eye diagrams for 20 Gb/s back-to-back NRZ 2^7–1 PRBS modulation at 25 and 85 °C. The bias current and modulation voltage were kept constant at 13 mA and 0.8 $V_{p\text{-}p}$ for this comparison. Both eyes are clearly open. The signal to noise ratio (S/N) changed only from 5.9 at 25 °C to 4.3 at 85 °C, the extinction ratio was above 4.0 dB. Fig. 11b shows the bit-error-rates (BER) also at 25 and 85 °C. Except for the modulation voltage at 25 °C of 1.2 $V_{p\text{-}p}$, the driving conditions were identical to the eye measurements. To account for the required discriminator voltage of the error detector, a 40 GHz amplifier was used after the photoreceiver. The device operates error free with a BER < 10^{-12} and no error floor even for 85 °C. The penalty at 85 °C is only 1 dB compared to the back-to-back error rate at 25 °C. As can be deduced from the error free eye in Fig. 19a at 25 °C, an identical modulation voltage of 0.8 $V_{p\text{-}p}$ would have resulted in the same BER, but the penalty at 85 °C compared to 25 °C would have been even smaller. To the best of our knowledge this is the fastest error free large signal modulation of any VCSEL at 85 °C. 20 Gb/s [3], [44] or faster [4] large signal modulation experiments have been performed at lower temperatures, but the high speed performance at 85 °C is crucial for most short-distance optical interconnect applications.

Thus, we demonstrated 980 nm VCSELs based on a triple stack of quantum dots, deposited in a submonolayer growth mode, with a thermally limited, error free 20 Gb/s direct modulated operation at 25 and 85 °C. In combination with their excellent static performance, i.e. high external efficiency even at 85 °C, these devices demonstrate the potential of this novel active material for temperature stable ultra high speed VCSELs. At room

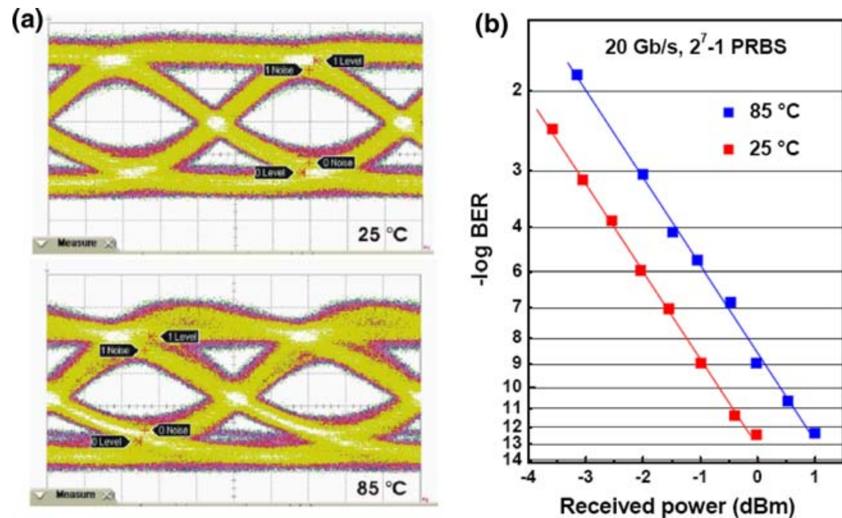

Fig. 19 (**a**) 20 Gb/s back-to-back eye diagram for a 6 μm SML QD-VCSEL at 25 and 85 °C without change of the bias current and modulation voltage and (**b**) bit-error-rate at 20 Gb/s back-to-back with 2^7-1 PRBS at 25 and 85 °C for the same bias current

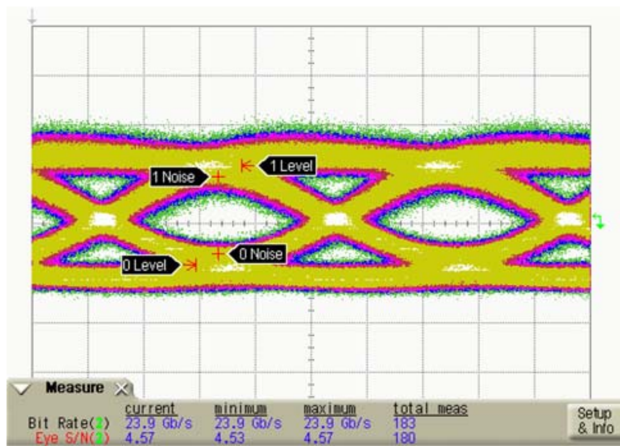

Fig. 20 Eye diagram at 24 Gb/s of SML-QD VCSEL at 25 °C

temperature, it is possible to achieve 25 Gb/s transmission (see Fig. 20) even both RC and photodetector response limitations (~25 GHz) become evident.

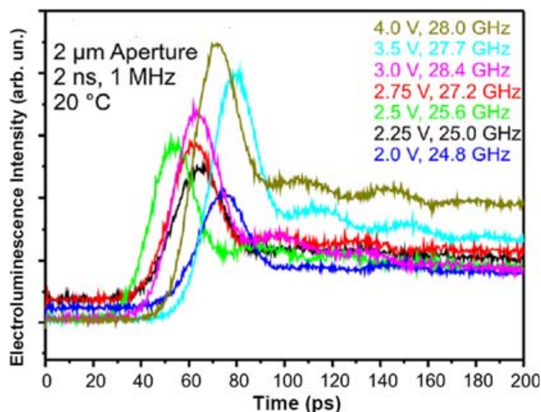

Fig. 21 Relaxation oscillations in the SML QD VCSEL as a function of bias voltage applied

To evaluate the ultimate time response of the device relaxation oscillation studies have been performed. A saturation relaxation oscillation frequency of 28 GHz was derived (see Fig. 21). Thus, >40 Gb/s transmission is possible in case if the device resistance is further reduced, and an optimized heat dissipating VCSEL design [45] is provided.

Conclusions

Development of novel types of QD media capable to ultrahigh current densities without suffering from gain saturation and lifetime degradation effects is a must to realize ultrahigh-speed directly modulated high-temperature VCSELs. SML QDs provide such an opportunity. The performance of SML QDs can be additionally enhanced by properly engineered VCSEL design. A significant further improvement in the performance of directly modulated VCSEL can be expected with proper optimization of SML QDs. Future work will also include wavelength adjustment of SML QDs to 850 nm and 1300 nm spectral ranges.

Acknowledgment The authors appreciate support from the German Ministry for Education and Research bmb+f (NanOp), the State of Berlin (TOB), the SANDiE Network of Excellence of the European Commission (NMP4-CT-2004–500101), NL-Nanosemiconductor (Innolume) GmbH and Discovery Semiconductors Inc. NJ.

References

1. G.K. Cambron "The multimedia explosion: transforming the physical layer" presented at the OFC/NFOEC 2006, March 5–10, 2006 Anaheim, California, USA
2. K.J. Ebeling, R. Michalzik, R. King, P. Schnitzer, D. Wiedenmann, R. Jäger, C. Jung, M. Grabherr, M. Miller, Proceedings of the 24th European Conference on Optical Communication, Madrid, Spain, 20–24 (IEEE, New York), vol. 3, (1998)

3. F.E. Doany, L. Schares, C.L. Schow, C. Schuster, D.M. Kuchta, P.K. Pepeljugoski et al., Proc. OFC/NFOEC 2006, OFA3 (2006)
4. N. Suzuki, H. Hatakeyama, K. Fukatsu, T. Anan, K. Yashiki, M. Tsuji, Proc. OFC/NFOEC 2006, OFA4 (2006)
5. D. Bimberg, M. Grundmann, N.N. Ledentsov, *Quantum Dot Heterostructures.* (Wiley, New York, 1998)
6. V. Shchukin, N.N. Ledentsov, D. Bimberg, *Epitaxy of Nanostructures, Springer Series in NanoScience and Technology*. Vol. XII (Springer, New York, 2004)
7. N.N. Ledentsov, V.M. Ustinov, A.Yu. Egorov, A.E. Zhukov, M.V. Maximov, I.G. Tabatadze, P.S. Kop'ev, Semiconductors. **28**, 832 (1994)
8. N. Kirstaedter, N.N. Ledentsov, M. Grundmann, D. Bimberg, V.M. Ustinov, S.S. Ruvimov, M.V. Maximov, P.K. Kop'ev, Zh.I. Alferov, U. Richter, P. Werner, U. Gosele, J. Heydenreich, Electron. Lett. **30**, 1416 (1994)
9. H. Shoji, K. Mukai, N. Ohtsuka, M. Sugawara, T. Uchida, H. Ishikawa, Photonics Technol. Lett. **7**, 1385 (1995)
10. N.N. Ledentsov, N. Kirstaedter, D. Bimberg, Photonics Technol. Lett. **8**, 1276 (1996)
11. H. Shoji, K. Mukai, T. Ohtsuka, M. Sugawara, T. Uchida, H. Ishikawa, Photonics Technol. Lett. **8**, 1277 (1996)
12. D.L. Huffaker, L.A. Graham, D.G. Deppe, Electronics Lett. **33**, 1225 (1997)
13. J.A. Lott, N.N. Ledentsov, V.M. Ustinov, A.Yu. Egorov, A.E. Zhukov, P.S. Kop'ev, Zh.I. Alferov, D. Bimberg, Electron. Lett. **33**, 1150 (1997)
14. F. Hopfer, I. Kaiander, A. Lochmann, A. Mutig, S. Bognar, M. Kuntz, U.W. Pohl, V.A. Haisler, D. Bimberg Appl. Phys. Lett. **89**, 061105 (2006)
15. J.A. Lott, N.N. Ledentsov, V.M. Ustinov, N.A. Maleev, A.E. Zhukov, A.R. Kovsh, M.V. Maximov, B.V. Volovik, Zh.I. Alferov, D. Bimberg, Electron. Lett. **36**, 1384 (2000)
16. M. Laemmlin, G. Fiol, M. Kuntz, F. Hopfer, A. Mutig, N.N. Ledentsov, A.R. Kovsh, C. Schubert, A. Jacob, A. Umbach, D. Bimberg, Physica Status Solidi (c). **3**, 391 (2006)
17. N. Hatory, K. Otsubo, M. Ishida, T. Akiyama, Y. Nakata, H. Ebe, S. Okumura, T. Yamamoto, M. Sugawara, Y. Arakawa, Extended Abstract. The 30th European Conference on Optical Communication, ECOC-2004, Stockholm, Sweden, 5–9 September 2004
18. Y.H. Chang, P.C. Peng, W.K. Tsai, G. Lin, F. Lai, R.S. Hsiao, H.P. Yang, H.C. Yu, K.F. Lin, J.Y. Chi, S.C. Wang, H.C. Kuo, Photonics Technol. Lett. **18**, 847 (2006)
19. C. Ribbat, R. Sellin, M. Grundmann, D. Bimberg, N.A. Sobolev, M.C. Carmo, Electron. Lett. **37**, 174 (2001)
20. I. Krestnikov, D. Livshits, S. Mikhrin, A. Kozhukhov, A. Kovsh, N. Ledentsov, A. Zhukov, Electron. Lett. **41**, 1330 (2005)
21. O.B. Shchekin, J. Ahn, D.G. Deppe, Electron. Lett. **38**, 712 (2002)
22. S.S. Mikhrin, A.R. Kovsh, I.L. Krestnikov, A.V. Kozhukhov, D.A. Livshits, N.N. Ledentsov, Yu.M. Shernyakov, I.I. Novikov, M.V. Maximov, V.M. Ustinov, Zh.I. Alferov, Semicond. Sci. Technol. **20**, 340 (2005)
23. V.I. Marchenko, Soviet Phys.—J. Exper. Theor. Phys. Lett. **33**, 381 (1981)
24. M. Tsuchiya, J.M. Gaines, R.H. Yan, R.J. Simes, P.O. Holtz, L.A. Coldren, P.M. Petroff, Phys. Rev. Lett. **62**, 466 (1989)
25. O. Brandt, L. Tapfer, K. Ploog, R. Bierwolf, M. Hohenstein, F. Phillipp, H. Lage, A. Heberle, Phys. Rev. B. **44**, 8043 (1991)
26. V. Bressler-Hill, A. Lorke, S. Varma, P.M. Petroff, K. Pond, W.H. Weinberg, Phys. Rev. B. **50**, 8479 (1994)
27. N.N. Ledentsov, I.L. Krestnikov, M.V. Maximov, S.V. Ivanov, S.L. Sorokin, P.S. Kopev, Zh.I. Alferov, D. Bimberg, N.N. Ledentsov, C.M. Sotomayor Torres, Appl. Phys. Lett. **69**, 1343 (1996), ibid. **70**, 2766 (1997)
28. I.L. Krestnikov, N.N. Ledentsov, A. Hoffmann, D. Bimberg, Phys. Stat. Sol. (a). **183**, 207 (2001)
29. I.L. Krestnikov, M. Straßburg, M. Caesar, A. Hoffmann, U.W. Pohl, D. Bimberg, N.N. Ledentsov, P.S. Kop'ev, Zh.I. Alferov, D. Litvinov, A. Rosenauer, D. Gerthsen, Phys. Rev. B. **60**, 8695 (1999)
30. V.A. Shchukin, D. Bimberg, Rev. Mod. Phys. **71**, 1125 (1999)
31. V.A. Shchukin, N.N. Ledentsov, A. Hoffmann, D. Bimberg, I.P. Soshnikov, B.V. Volovik, V.M. Ustinov, D. Litvinov, D. Gerthsen, Phys. Stat. Sol. (b). **224**(2), 503–508 (2001)
32. P. Yu, W. Langbein, K. Leosson, J.M. Hvam, N.N. Ledentsov D. Bimberg, V.M. Ustinov, A.Yu. Egorov, A.E. Zhukov, A.F. Tsatsulnikov, Yu.G. Musikhin, Phys. Rev. B. **60**, 16680 (1999)
33. T. Kita, O. Wada, H. Ebe, Y. Nakata, M. Sugawara, Jpn. J. Appl. Phys. Part 2 **41**, L1143 (2002)
34. F. Hopfer, A. Mutig, G. Fiol, M. Kuntz, V.A. Shchukin, V.A. Haisler, T. Warming, E. Stock, S.S. Mikhrin, I.L. Krestnikov, D.A. Livshits, A.R. Kovsh, C. Bornholdt, A. Lenz, H. Eisele, M. Dähne, N.N. Ledentsov, D. Bimberg, J. Sel. Topics Quantum Electron, in print
35. V.A. Shchukin, D. Bimberg, V.G. Malyshkin, N.N. Ledentsov, Phys. Rev B. **57**, 12262 (1998)
36. G. Springholz, V. Holy, M. Pinczolits, P. Mayer, V. Holy, G. Bauer, H.H. Kang, L. Salamanca-Riba, Phys. Rev. Lett. **84**, 4669 (2000)
37. O. Stier, M. Grundmann, D. Bimberg, Phys. Rev. B. **59**, 5688 (1999)
38. N.N. Ledentsov, V. Shchukin, "Optoelectronic device based on an antiwaveguiding cavity" United States Patent Application 20050226294
39. N.N. Ledentsov, F. Hopfer, A. Mutig, V.A. Shchukin, A.V. Savel'ev, G. Fiol, M. Kuntz, V.A. Haisler, T. Warming, E. Stock, S.S. Mikhrin, A.R. Kovsh, C. Bornholdt, A. Lenz, H. Eisele, M. Dähne, N.D. Zakharov, P. Werner, D. Bimberg Proc. SPIE Vol. 6468, 64681O, Physics and Simulation of Optoelectronic Devices XV; M. Osinski, F. Henneberger, Y. Arakawa, eds. (2007)
40. D.L. Huffaker, J. Shin, D.G. Deppe, Electron. Lett. **30**, 1946 (1994)
41. L.A. Coldren, S.W. Corzine, *Diode Lasers and Photonic Integrated Circuits, Wiley Series in Microwave and Optical Engineering*. vol. XXVI (Wiley, New York, 1995), p. 204
42. R. Stevens, R. Schatz, A. Lövqvist, T. Aggerstam, C. Carlsson, C.A. Barrios, S. Lourdudoss, M. Ghisoni, Proc. SPIE. **4286**, 71 (2001)
43. S.M. Kim, Y. Wang, M. Keever, J.S. Harris, IEEE Photon. Technol. Lett. **16**, 377 (2004)
44. P. Pepeljugoski, D. Kuchta, Y. Kwark, P. Pleunis, G. Kuyt, IEEE Photon. Technol. Lett. **14**, 717 (2002)
45. A.N. AL-Omari, G.P. Carey, S. Hallstein, J.P. Watson, G. Dang, K.L. Lear, IEEE Photon. Technol. Lett. **18**, 1225 (2006)